ADVANCED MATERIALS INTERFACES
Open Access
www.advmatinterfaces.de

Substrate-Dependent Anisotropy and Damping in Epitaxial Bismuth Yttrium Iron Garnet Thin Films

Takian Fakhrul, Bharat Khurana, Hans Toya Nembach, Justin M. Shaw, Yabin Fan, Grant A. Riley, Luqiao Liu, and Caroline A. Ross**

Iron garnets that combine robust perpendicular magnetic anisotropy (PMA) with low Gilbert damping are desirable for studies of magnetization dynamics as well as spintronic device development. This paper reports the magnetic properties of low-damping bismuth-substituted iron garnet thin films ($Bi_{0.8}Y_{2.2}Fe_5O_{12}$) grown on a series of single-crystal gallium garnet substrates. The anisotropy is dominated by magnetoelastic and growth-induced contributions. Both stripe and triangular domains form during field cycling of PMA films, with triangular domains evident in films with higher PMA. Ferromagnetic resonance measurements show damping as low as 1.3×10^{-4} with linewidths of 2.7 to 5.0 mT. The lower bound for the spin-mixing conductance of BiYIG/Pt bilayers is similar to that of other iron garnet/Pt bilayers.

1. Introduction

Iron garnets are ferrimagnetic insulators with composition $A_3Fe_5O_{12}$, where the dodecahedral A-sites are occupied by a rare earth (RE), Y, Bi, and so on. Films of many iron garnets such as $Tm_3Fe_5O_{12}$ can be grown with PMA as a result of magnetoelastic anisotropy,[1–3] which is useful in a range of spintronic device applications.[4] Iron garnets also exhibit fast magnetization dynamics due to their low Gilbert damping (α). Yttrium iron garnet (YIG) has the lowest damping among known magnetic materials,[5,6] and all the RE iron garnets (REIGs) exhibit larger values.[7,8] For bulk YIG, values of α as low as 10^{-5} have been reported, whereas for thin films of YIG, $\alpha = 6 \times 10^{-5}$ in the best case[9] and commonly $\alpha = (1–2) \times 10^{-4}$, as summarized in ref. [10]. The ferromagnetic resonance (FMR) full width at half maximum linewidth (FWHM) of YIG films is $\mu_0 \Delta H_0 = (0.4–0.6)$ mT.[10] A combination of PMA and low α is advantageous, but it is challenging to grow YIG thin films with PMA. PMA YIG films have been obtained by the use of buffer layers of $Sm_3Ga_5O_{12}$[11] or by growth on gadolinium scandium gallium garnet substrates ($Gd_3Sc_2Ga_3O_{12}$) to increase magnetoelastic anisotropy.[12] The latter experiment yielded $\alpha = (4–11) \times 10^{-4}$ and FWHM $\mu_0 \Delta H_0 = (1$ to $4)$ mT measured in an out-of-plane field. Bismuth-substituted yttrium iron garnet (BiYIG, $Bi_xY_{3-x}Fe_5O_{12}$) combines PMA and a moderately low damping, intermediate between that of YIG and REIGs. Soumah et al.[13] reported Bi_1Y_2IG with PMA grown on substituted gadolinium gallium garnet (SGGG, $Gd_{2.6}Ca_{0.4}Ga_{4.1}Mg_{0.25}Zr_{0.65}O_{12}$) with damping of $\alpha = 3 \times 10^{-4}$ and FWHM $\mu_0 \Delta H_0 = 0.40$ mT measured at an ≈27° angle from the in-plane direction at frequencies up to 20 GHz. The linewidth was over two orders of magnitude higher for an in-plane measurement. Lin et al. reported PMA Bi_1Y_2IG grown on SGGG with $\alpha = 7.03 \times 10^{-4}$[14] and peak-to-peak linewidth of 2 mT (i.e., FWHM = 3 mT) measured out-of-plane in the

T. Fakhrul, B. Khurana, Y. Fan, C. A. Ross
Department of Materials Science and Engineering
Massachusetts Institute of Technology
Cambridge, MA 02139, USA
E-mail: takianf@mit.edu; caross@mit.edu

T. Fakhrul
Department of Materials and Metallurgical Engineering
Bangladesh University of Engineering and Technology
Dhaka 1000, Bangladesh

H. T. Nembach, G. A. Riley
Associate, Physical Measurement Laboratory
National Institute of Standards and Technology
Boulder, CO 80305, USA

H. T. Nembach
Department of Physics
University of Colorado Boulder
Boulder, CO 80309, USA

J. M. Shaw
National Institute of Standards and Technology
Boulder, CO 80305, USA

Y. Fan, L. Liu
Department of Electrical Engineering and Computer Science
Massachusetts Institute of Technology
Cambridge, MA 02139, USA

G. A. Riley
Center for Memory and Recording Research
University of California-San Diego
La Jolla, CA 92093, USA

The ORCID identification number(s) for the author(s) of this article can be found under https://doi.org/10.1002/admi.202300217

DOI: 10.1002/admi.202300217

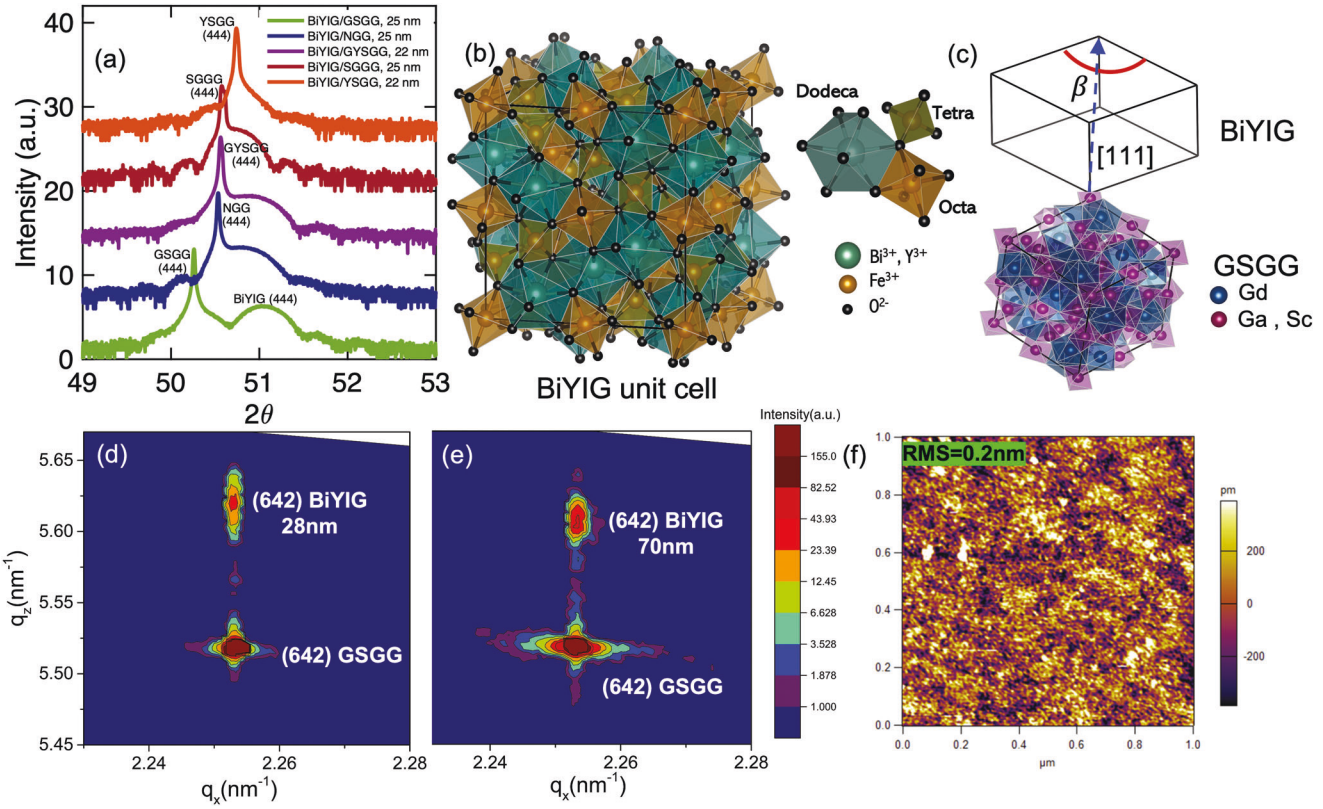

Figure 1. a) HRXRD ω–2Θ scans around the BiYIG (444) and GSGG, NGG, GYSGG, SGGG, and YSGG (444) peaks. b) Cubic unit cell of BiYIG showing octahedrally, tetrahedrally, and dodecahedrally-coordinated cation sites. The cation sites are surrounded by O^{2-} (indicated by black spheres) at the vertices of the polyhedra. c) Schematic of a strained BiYIG cubic unit cell on GSGG with the corner angle β marked. d,e) HRXRD reciprocal-space map of 28 nm BiYIG/GSGG (d) and 70 nm BiYIG/GSGG (e). f) AFM scan on 7 nm thick BiYIG film on GSGG.

frequency range of 6–13 GHz.

In this work, we report the structure, magnetic properties, and FMR characterization of BiYIG films that are grown epitaxially on a range of (111)-oriented garnet substrates with varying lattice parameters. In FMR, a limited frequency range for damping measurements can lead to nonlinearities in linewidth as reported in both metallic systems[15] and YIG[16] owing to a slow-relaxing impurity mechanism and low-field losses. We therefore carry out FMR measurements at frequencies up to 40 GHz, obtaining damping as low as 1.3×10^{-4} and inhomogeneous broadening FWHM linewidth of 2–5 mT for an out-of-plane field. The domain structure and reversal characteristics of the films are investigated by MOKE imaging. Finally, a lower bound for the spin-mixing conductance is reported for BiYIG/Pt bilayers, which is comparable with previous reports of spin-mixing conductance in PMA REIG/Pt bilayers.

2. Results and Discussion

2.1. Structure and Magnetic Anisotropy

BiYIG films ranging from 20–70 nm in thickness were grown by pulsed laser deposition (PLD) on (111)-oriented substituted gadolinium gallium garnets of composition $Y_3Sc_2Ga_3O_5$ (YSGG), SGGG, $Gd_3Sc_2Ga_3O_{12}$ (GSGG), $Gd_{0.63}Y_{2.37}Sc_2Ga_3O_{12}$ (GYSGG), and neodymium gallium garnet ($Nd_3Ga_5O_{12}$, NGG). The bulk lattice parameters of YSGG, SGGG, NGG, GYSGG, and GSGG were 1.2426, 1.2480, 1.2505, 1.2507, and 1.2554 nm, respectively, all larger than that of $Gd_3Ga_5O_{12}$ (GGG) of 1.2375 nm. BiYIG films grown on these substrates therefore exhibit a range of epitaxial strains and magnetoelastic anisotropy. The target used for the thin film growth had a composition of $Bi_{0.8}Y_{2.2}Fe_5O_{12}$. An analysis of the growth conditions that gave high quality epitaxial BiYIG film is given in our previous work,[17–19] and optimized conditions used in the present work can be found in the Experimental Section. Bi has a larger ionic radius than Y and it causes an expansion of 0.0083 nm per Bi atom substituted in the formula unit.[20]

Figure 1a shows high resolution X-ray diffraction (HRXRD) $2\theta - \omega$ data for BiYIG films grown on GSGG, NGG, GYSGG, SGGG, and YSGG. The well-defined Laue fringes indicate the high crystalline quality and uniformity of the BiYIG films. Both the unstrained and strained unit cell of BiYIG are shown in Figure 1b,c, where the three different lattice sites for the cations with respect to O^{2-} are indicated. Reciprocal-space mapping (RSM) for the (642) reflection shows that all the BiYIG films up to 70 nm thick on GSGG, NGG, and SGGG were lattice matched to the substrate. RSM for 28.3 and 70 nm thick BiYIG films on GSGG is shown in Figure 1d,e. We conclude that the films are under in-plane tensile strain, and the unit cell of the BiYIG is distorted from cubic to rhombohedral (Figure 1c). A rhombohedral-to-hexagonal transformation was used to simplify the calculation

of the strain tensor as detailed in our previous work.[21] The in-plane lattice parameter a_H and the c-axis lattice parameter c of the hexagonal unit cell are given by $a_H = \sqrt{12d_{11\bar{2}}^2}$ and $c = 12d_{444}$. Here, $d_{11\bar{2}}$ is the $(11\bar{2})$ plane spacing of the BiYIG cubic unit cell which is assumed to match the substrate $(11\bar{2})$ plane spacing and d_{444} is the spacing of the (444) planes. The corner angle β of the strained unit cell as shown in Figure 1c is given by $\sin\left(\frac{\beta}{2}\right) = \frac{3}{2\sqrt{3+\left(\frac{c}{a_H}\right)^2}}$.

Atomic force microscopy (AFM) shows that the BiYIG films have a root mean square (RMS) surface roughness of less than 0.2 nm (Figure 1f). High-resolution high-angle annular dark-field scanning transmission electron microscopy (HAADF STEM) images of 7 nm thick BiYIG grown on GSGG were described in our prior publication[22] and indicate epitaxial growth without visible dislocations or other interfacial defects.

The magnetic hysteresis loops of the films were characterized by vibrating sample magnetometry (VSM). Measurements with field applied in-plane (IP) and out-of-plane (OP) are shown in **Figure 2** a–f. The films grown on GSGG and NGG demonstrate PMA with square OP hysteresis loops whereas films grown on SGGG have an IP easy axis. BiYIG films grown on NGG, YSGG, and GYSGG show OP coercivity of ≈1.6 kA m^{-1} and films on GSGG have higher coercivity of 8.0 kA m^{-1}. The saturation magnetization of BiYIG was (135 ± 10) kA m^{-1} for thicknesses of 20–70 nm on all the substrates. The large paramagnetic background signal of the GSGG, NGG, and SGGG substrates prevented background subtraction for the hard axis loops of most of the BiYIG films, and net anisotropy was measured using FMR as described below.

The total magnetic anisotropy of the films includes contributions from magnetocrystalline, shape, magnetoelastic, and growth-induced anisotropy. The total uniaxial anisotropy K_u of the films was given by the difference between the magnetic energy E when the magnetization was oriented IP versus OP:

$$K_u = E_{IP} - E_{OP} = K_{mc} + K_{me} + K_{sh} + K_g$$
$$= -\frac{K_1}{12} + \frac{9}{4}\lambda_{111}c_{44}\left(\frac{\pi}{2} - \beta\right) - \frac{\mu_o}{2}M_s^2 + K_g \quad (1)$$

Here, K_{mc} is the magnetocrystalline, K_{sh} the shape, K_{me} the magnetoelastic, and K_g the growth-induced anisotropy. K_1 is the first order cubic magnetocrystalline anisotropy constant, M_s is the saturation magnetization, λ_{111} is the magnetostriction coefficient, c_{44} is the shear modulus, and β is the corner angle of the rhombohedrally-distorted unit cell. A positive K_u corresponds to an out-of-plane easy axis. K_1 for BiYIG is negative which favors PMA for (111) films, but this contribution is small (≈ −650 Jm^{-3}[23]); and thus, the magnetocrystalline anisotropy will be neglected. The shape anisotropy $\left(-\frac{\mu_o}{2}M_s^2\right)$ favors in-plane magnetization.

K_{me} is proportional to both λ_{111} and the shear strain $\left(\frac{\pi}{2} - \beta\right)$. The magnitude of λ_{111} is linearly dependent on the Bi content according to[23] $\lambda_{111}\ (Bi_zY_{3-z}IG) = -2.73 \times 10^6\ (1 + 0.23z)$. The higher magnetostriction of BiYIG compared to YIG is attributed to an increase in the spin-orbit coupling due to mixing between the 6p Bi^{3+} orbitals and the 3d and 2p orbitals from $Fe^{3+}$and O^{2-}.[23] The $\lambda_{111}$for BiYIG is negative; and therefore, favors an easy axis along the compressively strained OP direction, promoting PMA in BiYIG films grown on larger lattice parameter substrates. Thus, magnetoelastic anisotropy contributes to PMA in BiYIG films grown on substrates with larger lattice parameter than that of the film.

Like Soumah et al.,[13] we find that magnetoelastic anisotropy alone is insufficient to account for the PMA in our BiYIG films, as shown in **Table 1**. We observe an increase in β with increasing substrate lattice parameter, as expected. However, the net anisotropy does not increase monotonically with the strain. In fact, the magnetoelastic contribution is a relatively small part of the total anisotropy, leading to the conclusion that the growth-induced anisotropy is dominant. Partially substituted garnet films like BiYIG exhibit K_g due to the non-random distribution of Bi^{3+} and Y^{3+} in nonequivalent dodecahedral sites, driven by the ionic size difference. Growth-induced anisotropy has been analyzed in mixed rare earth and other mixed composition garnets grown by liquid phase epitaxy (LPE),[24–28] and more recently, in PLD-grown (Tm,Y)IG.[29] It leads to an uniaxial magnetic anisotropy term in (111)-oriented (and (001)-oriented) films. The magnitude and the sign of K_g depend on the ions present and their atomic fraction, and for Bi^{3+} substitution in YIG, K_g favors PMA.[30] In LPE-grown Bi-containing $(Y,Lu)_3Fe_5O_{12}$, the addition of Bi can increase K_g by an order of magnitude.[31] We calculate K_g from the total anisotropy K_u after subtracting the shape and magnetoelastic contributions. BiYIG on GSGG and NGG have very large growth-induced anisotropies while films on SGGG, GYSGG, and YSGG have lower growth-induced anisotropy and an in-plane easy axis as shown in Figure 2. K_g calculated for the PLD-grown BiYIG in Table 1 varies with substrate and film thickness, and in many samples, it exceeds that of LPE-grown garnets[25–28,32] and PLD-grown (Tm,Y)IG.[29]

2.2. Domain Imaging

Magneto-optical Kerr effect (MOKE) microscopy was carried out on PMA BiYIG films with thicknesses 25, 28, and 33 nm grown on GSGG substrates, and 25 and 27 nm grown on NGG substrates. All the films were a.c. demagnetized using an electromagnet with an alternating OP magnetic field with an initial value of $\mu_0 H = 500$ mT and a reduction ratio of 0.95 between each step. MOKE images for the resulting domain structures for these films are shown in **Figure 3**. After demagnetization, the net magnetization is close to zero and up and down domains occupy roughly equal areas. The average domain size was calculated using images taken from multiple locations on each film and is displayed in Table 1. The large standard deviations in the domain sizes are indicative of heterogeneities in the domain structures in different regions of the samples.

MOKE images for a.c. demagnetized films with thickness 25 nm grown on GSGG and 25 and 27 nm grown on NGG show a labyrinthine domain structure, Figure 3a,d,e. In comparison, 28 and 33 nm BiYIG films on GSGG show triangular domains indicating preferential formation of domain walls along certain crystallographic directions. (Figure 3b,c). The two films in our study that exhibited triangular domains also have higher lattice distortion β and higher K_{me} as well as higher K_g compared to similar thickness films with stripe domains. This suggests that

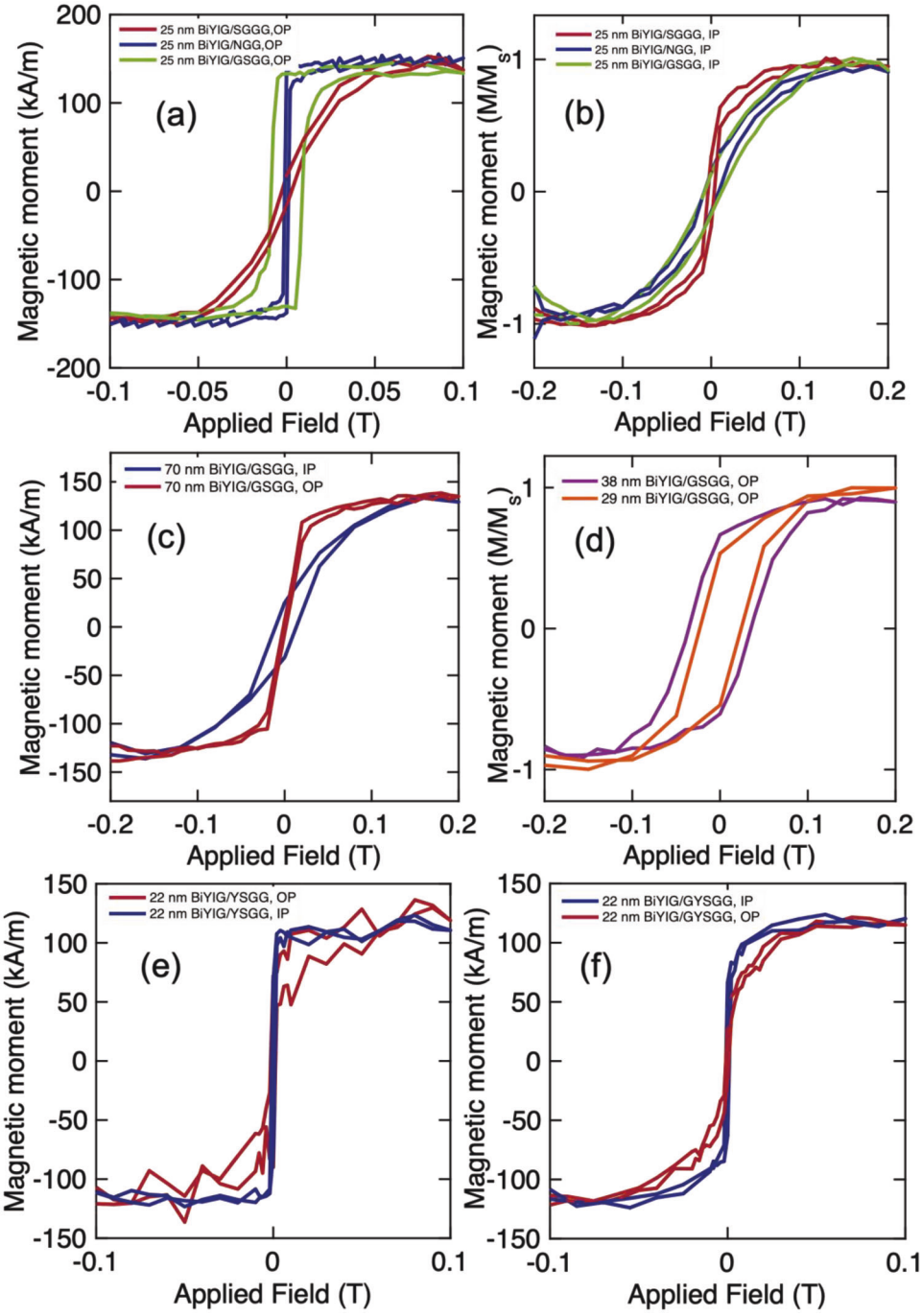

Figure 2. Hysteresis loops with field applied a) out-of-plane (OP) and b) in-plane (IP) for 25 nm BiYIG on SGGG, NGG, and GSGG. c) IP and OP loops for 70 nm BiYIG on GSGG. d) OP loops for 38 and 28 nm BiYIG on GSGG. e,f) IP and OP loops for 22 nm BiYIG on YSGG and GYSGG.

the domain shape correlates with strain state and anisotropy and has a different origin from the triangular domain structures reported in thin metal films.[33,34] There have been multiple reports of threading and misfit dislocation defects in micron-thickness BiYIG films due to lattice and thermal mismatch.[35–38] We speculate that localized strain relaxation accompanied by the formation of dislocations leads to crystallographically-preferred orientations for domain walls due to favorable interaction with their strain fields which can potentially result in anisotropy in the domain wall energy. The critical lattice mismatch causing the onset of triangular defects has been reported to be 4.1 pm (at growth temperatures) in REIGs and lower in Bi-substituted garnets.[35] At room temperature, our BiYIG/GSGG has a lattice misfit of 10.4 pm which is well above this threshold.

MOKE microscopy was used to study magnetization reversal for 28 and 70 nm thick BiYIG/GSGG and 25 nm BiYIG/NGG,

Table 1. Magnetic properties of BiYIG films on garnet substrates.

Film thickness [nm]	Substrate	PMA	β [°]	$K_u - K_{sh}$ [kJ m^{-3}]	K_{sh} [kJ m^{-3}]	K_{me} [kJ m^{-3}]	$K_{sh} + K_{me}$ [kJ m^{-3}]	K_g [kJ m^{-3}]	Domain shape	Domain size [μm]
22	YSGG	No	90	≈10.7	−10.7	0	−10.7	10.7	–	–
25	SGGG	No	90.1	11.1	−13.2	1.7	−11.5	9.4	–	–
25	NGG	Yes	90.2	29.1	−13.1	2.2	−10.9	26.9	Stripe	30 ± 9
27	NGG	Yes	90.3	25.5	−11.1	3.0	−8.1	22.5	Stripe	26 ± 8
22	GYSGG	No	90.3	≈9.8	−9.8	3.0	−6.8	6.8	–	–
25	GSGG	Yes	90.6	30.2	−9.8	5.8	−4.0	24.4	Stripe	32 ± 8
28	GSGG	Yes	90.7	49.2	−13.1	7.1	−6.0	42.1	Triangular	67 ± 22
32.9	GSGG	Yes	90.7	44.8	−13.2	7.1	−6.1	37.7	Triangular	84 ± 35
70	GSGG	Yes	90.6	17.9	−12.3	5.8	−6.5	12.1	Stripe	–

Figure 4. MOKE images were collected while applying an OP magnetic field of −60 mT, followed by an OP field sweep from 0 mT to a positive value to magnetize the film in the positive direction. The image collected at −60 mT was subtracted from all the subsequent images to remove the non-magnetic contrast.

Magnetization reversal for 70 nm BiYIG/GSGG and 25 nm BiYIG/NGG shown in Figure 4a,b proceeds by formation of labyrinthine stripe domains. A similar stripe domain structure has been reported for TmIG[39] and (Tm,Y)IG.[29] Magnetization reversal was almost complete at +15 mT for the 70 nm thick BiYIG/GSGG substrate and at +4 mT for the 25 nm thick BiYIG/NGG. However, magnetization reversal for the 28 nm thick BiYIG/GSGG proceeded by formation of triangular domains such as those observed in its a.c.-demagnetized state, along with stripe domains within the triangular regions as shown in Figure 4c. After applying −60 mT, the field was swept from 0 mT to +100 mT with 0.5 mT steps. The film did not reach positive saturation even at +100 mT. This agrees with the hysteresis loop of this film shown in Figure 2d, where the film is not saturated even at 200 mT. A supplementary video showing the images in 0.5 mT field increments from 0 to 100 mT has been included as Supporting Information.

2.3. Ferromagnetic Resonance Characterization

To extract the damping of the BiYIG thin films, their dynamic magnetic properties were studied with broadband perpendicular FMR spectroscopy based on the vector network analyzer (VNA) technique in the 10–40 GHz range.[40–43] The complex transmission parameter S_{21} was measured at a fixed frequency while the external perpendicular magnetic field was swept,[40] as shown in

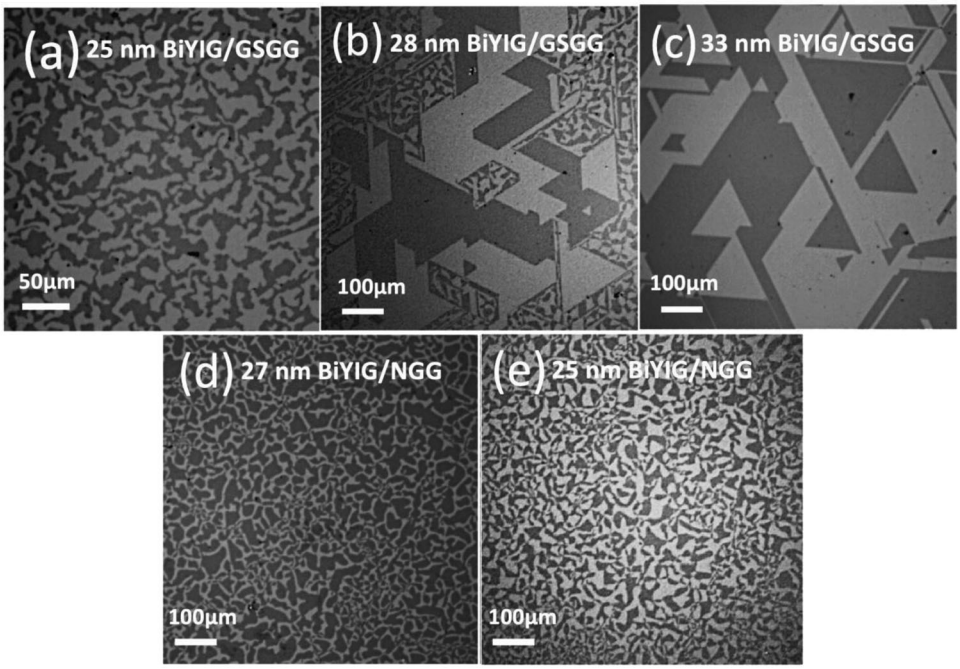

Figure 3. MOKE images showing equilibrium domain structure after a.c. demagnetization of a) 25 nm BiYIG/GSGG, b) 28 nm BiYIG/GSGG, c) 33 nm BiYIG/GSGG, d) 27 nm BiYIG/NGG, and e) 25 nm BiYIG/NGG.

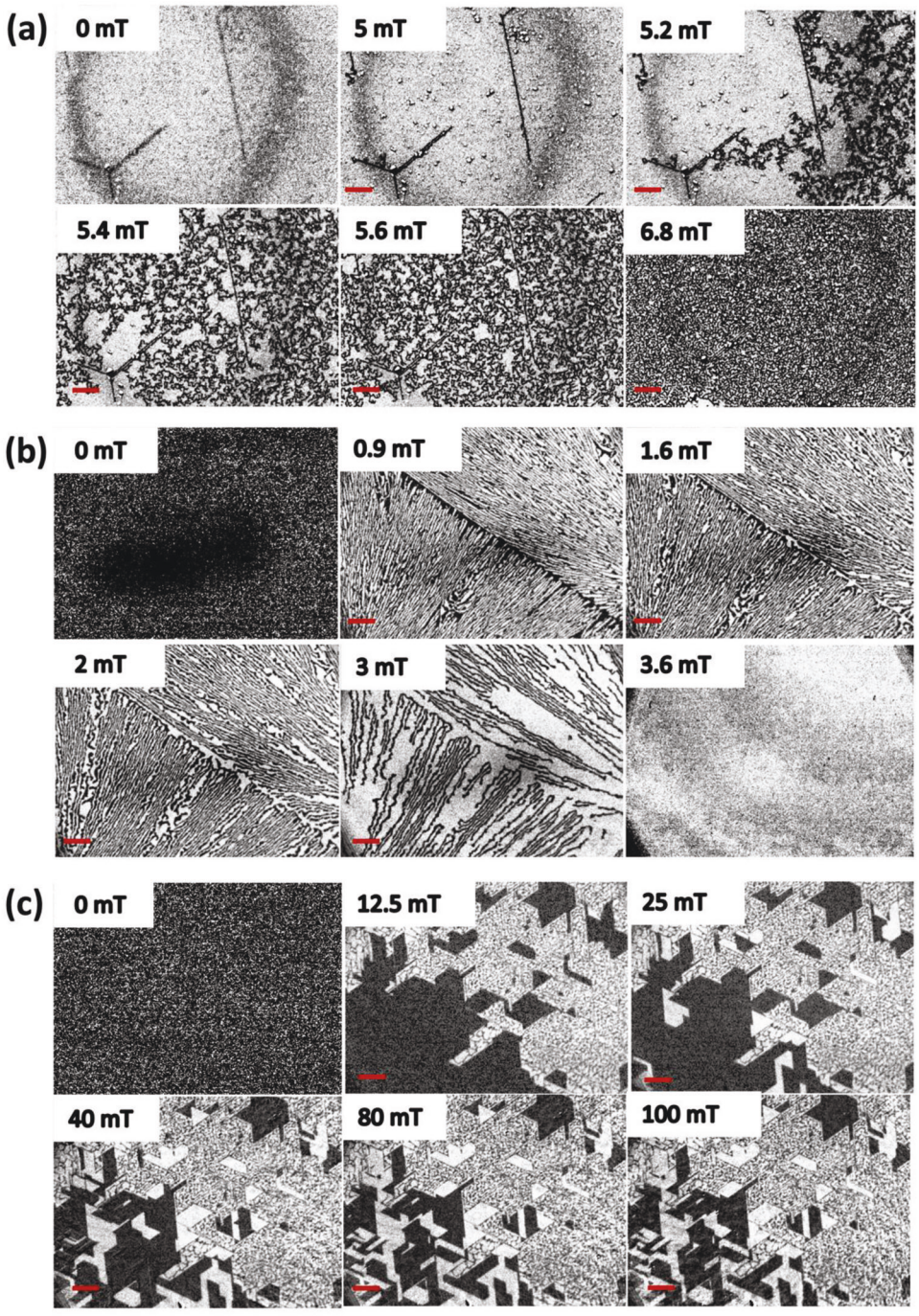

Figure 4. MOKE images showing domain structure during reversal of a) 70 nm BiYIG/GSGG, b) 25 nm BiYIG/NGG, and c) 28 nm BiYIG/GSGG. The films were saturated at +60 mT for (a) and −60 mT for (b,c). The red scale bar represents 100 µm.

Figure 5a,b. The resonance field for the films was fitted to the Kittel equation for perpendicular geometry to extract the effective magnetization M_{eff} and the Landé g-factor,[44] as shown in Figure 5c for one film as an example. Here:

$$H_{\text{res}} = \frac{2\pi \text{f}}{|\gamma|\,\mu_o} + M_{\text{eff}} \tag{2}$$

where H_{res} is the resonance field, f is the excitation frequency, and γ is the gyromagnetic ratio $(g\mu_{\text{B}})/h$, where μ_{B} is the Bohr magneton and h is the reduced Planck constant. The anisotropy of the film excluding the shape anisotropy, $K = K_{\text{u}} - K_{\text{sh}}$, is extracted from M_{eff} using the equation:[45,46]

$$M_{\text{eff}} = M_{\text{s}} - \frac{2K}{\mu_{\text{o}} M_{\text{s}}} \tag{3}$$

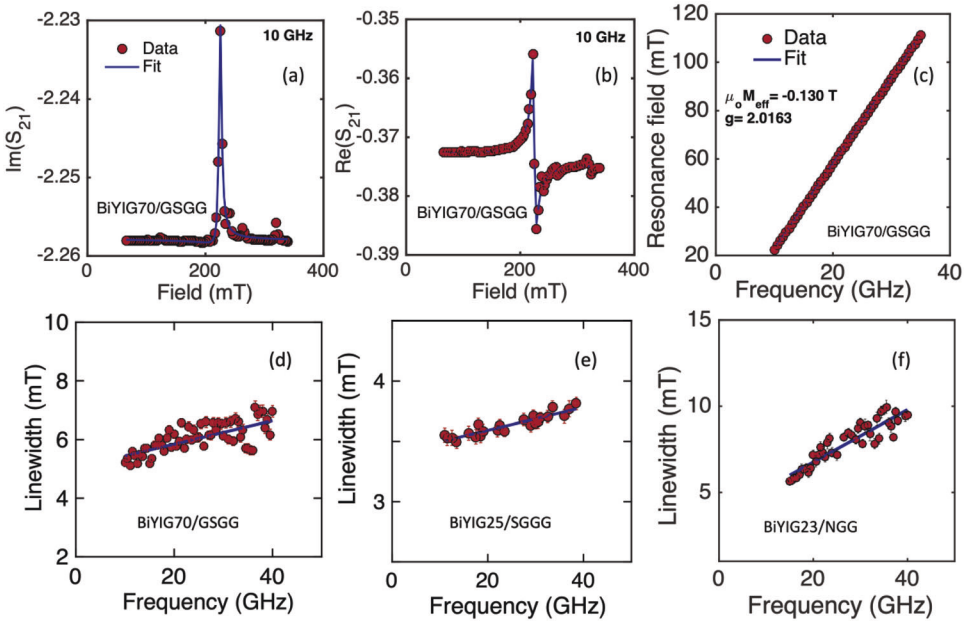

Figure 5. Representative FMR spectra taken at 10 GHz showing a) the imaginary and b) the real part of S_{21} for a 70 nm BiYIG/GSGG. c) Representative fit of the resonant field, H_{res}, versus frequency for 70 nm BiYIG/GSGG. FMR linewidth as a function of frequency for d) 70 nm BiYIG/GSGG, e) 25 nm BiYIG/SGGG, and f) 23 nm BiYIG/NGG.

The damping α and the inhomogeneous broadening FWHM linewidth ΔH_0 were extracted by fitting the linewidth to the following expression, Figure 5d–f:

$$\Delta H = \frac{4\pi\alpha f}{|\gamma|\,\mu_0} + \Delta H_0 \tag{4}$$

where ΔH is the experimentally observed linewidth determined from fitting the S_{21} data with the complex susceptibility. 25 nm BiYIG/SGGG yielded $\alpha = 1.3 \times 10^{-4}$ and $\mu_0 \Delta H_0 = 2.7$ mT. For 70 nm BiYIG/GSGG, $\alpha = 5.6 \times 10^{-4}$ and $\mu_0 \Delta H_0 = 5$ mT, and for 23 nm BiYIG/NGG, α was higher at 2.1×10^{-3}, with $\mu_0 \Delta H_0 = 3.7$ mT. No systematic change was observed with varying thickness or substrate, but the higher damping of BiYIG/NGG may correlate with the comparatively poorer crystalline quality of the as-supplied NGG substrates that led to growth of BiYIG with lower intensity Laue fringes. Our results confirm that low damping and moderately low linewidth of a few mT are achievable for BiYIG measured in the OP direction up to 40 GHz.

2.4. Spin-Mixing Conductance of BiYIG/Pt Interface

To characterize the efficiency of spin transport through the Pt/BiYIG interface, we measure the spin-mixing conductance of a bilayer of 4 nm Pt/4.3 nm BiYIG. A charge current in the Pt yields a spin current perpendicular to the film due to the spin Hall effect (SHE). The spin current is partially reflected at the garnet/heavy metal (HM) interface based on the relative orientation of the polarization of the spin current (σ) and the magnetization of the garnet (m). The real component of spin-mixing conductance $G_r^{\uparrow\downarrow}$ is associated with a damping-like torque which is proportional to $m \times (\sigma \times m)$, and the imaginary component of spin-mixing conductance $G_i^{\uparrow\downarrow}$ is associated with a field-like torque which is proportional to $\sigma \times m$.[47,48] The reflected spin current produces a charge current in the HM layer due to the inverse spin Hall effect; and thus, modulates the resistance of the HM layer leading to a spin Hall magnetoresistance (SMR). Longitudinal and transverse components of SMR are given by the following equations:[21,49]

$$R = R_0 + \Delta R^{\mathrm{SMR}} sin^2\theta\, sin^2\phi \tag{5}$$

$$R_{\mathrm{H}} = R_{\mathrm{H}}^{\mathrm{SMR}} sin^2\theta \sin 2\phi + R_{\mathrm{H}}^{\mathrm{AHE,\ SMR}} \cos\theta + R_{\mathrm{H}}^{\mathrm{OHE}} H_z \tag{6}$$

where R_0 is the m-independent longitudinal resistance of the HM layer and ΔR^{SMR} is its modulation due to SMR. $R_{\mathrm{H}}^{\mathrm{SMR}}$ and $R_{\mathrm{H}}^{\mathrm{AHE,\ SMR}}$ are the transverse components of SMR and anomalous Hall effect (AHE)-like SMR, respectively. $R_{\mathrm{H}}^{\mathrm{OHE}}$ is the contribution from the ordinary Hall effect (OHE) of the HM, H_z is the out-of-plane magnetic field, and θ and φ are the polar and azimuthal angles of m.[2] The Pt (4 nm)/BiYIG (4.3 nm)/NGG heterostructure was patterned into Hall cross devices and a probe station was used to perform transverse SMR measurements with an out-of-plane magnetic field. The Hall resistance for an OP field sweep from −15 to +15 mT is shown in **Figure 6**a after subtraction of a sample-dependent offset and linear OHE signal. The loop shows 100% remanence which agrees with the PMA observed from the VSM measurements. Sharp switching can be observed with a coercivity of (3 ± 0.5) mT. We obtained values of $R_{\mathrm{H}}^{\mathrm{AHE,\ SMR}} = -0.86$ mΩ and $R_{\mathrm{H}}^{\mathrm{OHE}} = -10.7$ mΩ T^{-1}, which gives $\rho_{xy}^{\mathrm{AHE,SMR}} = -3.44 \times 10^{-4}$ μΩ cm and $\rho_{xy}^{\mathrm{OHE}} = -4.28 \times 10^{-3}$ μΩ cm T^{-1}. The maximum magnitude of magnetic field available in the probe station was 100 mT which was not sufficient to saturate the film IP, precluding in-plane SMR measurements.

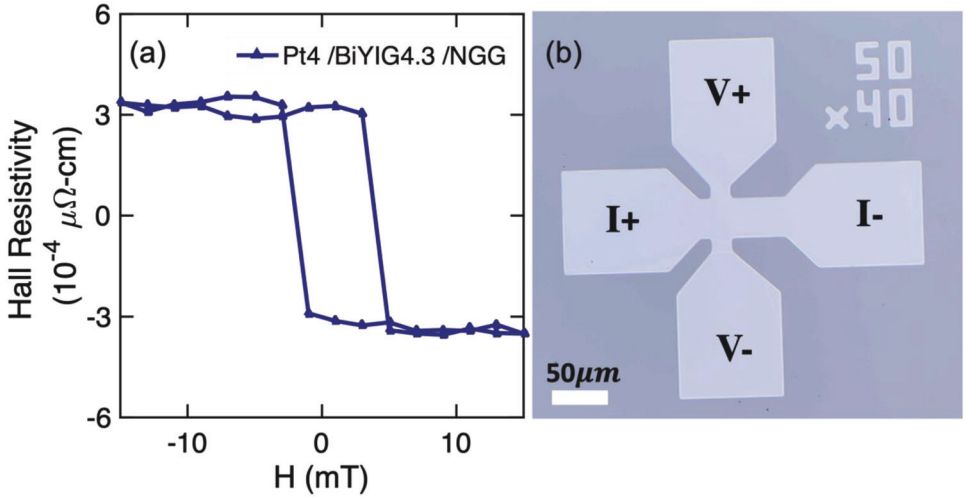

Figure 6. a) Anomalous Hall effect (AHE)-like spin Hall magnetoresistance (SMR) hysteresis loops for NGG(111)|BiYIG(4.3 nm)/Pt(4 nm) heterostructure. b) Optical micrograph of Hall cross used for measurement.

The model of Chen et al. for spin mixing conductance yields:[50]

$$\frac{\rho_{xy}^{\mathrm{SMR}}}{\rho_{xx}^{\mathrm{Pt}}} = \frac{\theta_{\mathrm{SH}}^2\,\lambda_{\mathrm{Pt}}}{d_{\mathrm{N}}}\,\frac{2\,\lambda_{\mathrm{Pt}}G_{\mathrm{r}}\tanh^2\frac{d_{\mathrm{N}}}{2\,\lambda_{\mathrm{Pt}}}}{\sigma_{xx}^{\mathrm{Pt}}+2\,\lambda_{\mathrm{Pt}}G_r\coth\frac{d_{\mathrm{N}}}{2\,\lambda_{\mathrm{Pt}}}} \tag{7}$$

$$\frac{\rho_{xy}^{\mathrm{AHE,SMR}}}{\rho_{xx}^{Pt}} = \frac{2\,\theta_{\mathrm{SH}}^2\,\lambda_{Pt}^2}{d_{\mathrm{N}}}\,\frac{\sigma_{xx}^{Pt}\,G_{\mathrm{i}}\tanh^2\frac{d_{\mathrm{N}}}{2\,\lambda_{\mathrm{Pt}}}}{\left(\sigma_{xx}^{\mathrm{Pt}}+2\,\lambda_{\mathrm{Pt}}G_r coth\frac{d_{\mathrm{N}}}{2\,\lambda_{\mathrm{Pt}}}\right)^2} \tag{8}$$

where ρ_{xy}^{SMR} and $\rho_{xy}^{\mathrm{AHE,SMR}}$ are Hall resistivities due to SMR and AHE-like SMR, respectively; $\rho_{xx}^{\mathrm{Pt}} = 47.1$ μΩ cm is the resistivity (and $\sigma_{xx}^{\mathrm{Pt}}$ is the conductivity) of Pt which we measure from the Hall bar, θ_{SH} is the spin-Hall angle of Pt, λ_{Pt} is the spin diffusion length in Pt, d_{N} is the thickness of the Pt layer = 4 nm, and G_{r} and G_{i} are the real and imaginary components of spin-mixing conductance. Without being able to achieve IP saturation for the film, we cannot obtain ρ_{xy}^{SMR}; and hence G_{r}. However, $\lambda_{\mathrm{Pt}}G_{\mathrm{r}}$ is generally much lower than $\sigma_{xx}^{\mathrm{Pt}}$.[51,52] Thus, if we drop G_{r} in the denominator of the second equation, we can obtain a lower bound for G_{i}. This value is 3.1×10^{12} Ω^{-1} m^{-2} for $\theta_{\mathrm{SH}} = 0.08$,[53] λ_{Pt} = 1.4 nm[50] or 6.1×10^{10} Ω^{-1} m^{-2} for $\theta_{\mathrm{SH}} = 0.387$,[53] and λ_{Pt} = 4.2 nm.[54] G_{i} is comparable to previous results reported for several REIG/Pt interfaces,[51] suggesting that the spin transport across the interface is dominated by the Fe sublattices.

3. Conclusion

Epitaxial BiYIG films with thicknesses ranging from 20 to 70 nm were grown by pulsed laser deposition from a target with composition $Bi_{0.8}Y_{2.2}Fe_5O_{12}$ onto several (111)-oriented single crystal garnet substrates with different lattice parameters. The films were coherently strained to the substrates and increasing the lattice parameter of the substrates promoted perpendicular magnetic anisotropy. Magnetoelastic anisotropy was insufficient to explain the net anisotropy, implying the presence of growth-induced anisotropy of 7–42 kJ m^{-3}, generally higher for more highly strained films. Most of the films exhibited stripe domains, but the films with highest anisotropy showed triangular domain patterns. We found a lower bound for the spin mixing conductance which was similar to that of other iron garnets, a damping of 1.3×10^{-4} to 2.1×10^{-3}, and an inhomogeneous broadening of $\mu_0 H_0 = 2.7$–5 mT for out-of-plane measurements up to 40 GHz. The low damping, tunable anisotropy, and high magnetooptical contrast were advantageous for a range of magnetooptical and spintronic applications and phenomena.

4. Experimental Section

BiYIG films ranging from 20 to 70 nm in thickness were grown by pulsed laser deposition (PLD) on (111) oriented substituted gadolinium gallium garnets YSGG, SGGG, NGG, GYSGG, and GSGG. The target used for the thin film growth had a composition of $Bi_{0.8}Y_{2.2}Fe_5O_{12}$. The chamber was pumped to 5×10^{-6} Torr base pressure prior to introducing oxygen and depositing the films. The laser repetition rate was 10 Hz, the laser fluence was ≈2 J cm^{-2}, and the target-substrate distance was 6 cm. The substrate temperature was 560 °C and the O_2 pressure was 20 Pa (150 mTorr). After growth, the samples were cooled down under 230 Torr of O_2. Pt was grown in a magnetron sputtering system at room temperature, with an Ar pressure of 0.26 Pa (2 mTorr). HRXRD measurements were performed using a Bruker D8 Discover HRXRD. For broadband perpendicular FMR spectroscopy based on the vector network analyzer technique, the samples were placed face-down on a 50 Ω coplanar waveguide. A static out-of-plane magnetic field up to 2.2 T was swept to saturate the film in the out-of-plane direction. A variable microwave field was applied in-plane while the microwave transmission at frequencies from 10–40 GHz was measured. Certain commercial instruments were identified to specify the experimental study adequately. This does not imply endorsement by NIST or that the instruments were the best available for the purpose.

Supporting Information

Supporting Information is available from the Wiley Online Library or from the author.

Acknowledgements

The authors acknowledge support from SMART, a nCORE Center of SRC and NIST, and NSF award 2028199. The shared facilities of MRSEC DMR 1419807 were used.

Conflict of Interest

The authors declare no conflict of interest.

Data Availability Statement

The data that support the findings of this study are available from the corresponding author upon reasonable request.

Keywords

damping, ferromagnetic resonance, garnet, perpendicular magnetic anisotropy

Received: March 14, 2023
Revised: July 3, 2023
Published online:

[1] A. S. Ahmed, A. J. Lee, N. Bagués, B. A. McCullian, A. M. Thabt, A. Perrine, P. K. Wu, J. R. Rowland, M. Randeria, P. C. Hammel, D. W. McComb, F. Yang, *Nano Lett.* **2019**, *19*, 5683.
[2] A. Quindeau, C. O. Avci, W. Liu, C. Sun, M. Mann, A. S. Tang, M. C. Onbasli, D. Bono, P. M. Voyles, Y. Xu, J. Robinson, *Adv. Electron. Mater.* **2017**, *3*, 1600376.
[3] C. O. Avci, E. Rosenberg, L. Caretta, F. Büttner, M. Mann, C. Marcus, D. Bono, C. A. Ross, G. S. Beach, *Nat. Nanotechnol.* **2019**, *14*, 561.
[4] E. Y. Vedmedenko, R. K. Kawakami, D. D. Sheka, P. Gambardella, A. Kirilyuk, A. Hirohata, C. Binek, O. C. Fesenko, S. Sanvito, B. J. Kirby, J. Grollier, *J. Phys. D: Appl. Phys.* **2020**, *53*, 453001.
[5] H. Chang, P. Li, W. Zhang, T. Liu, A. Hoffmann, L. Deng, M. Wu, *IEEE Magn. Lett.* **2014**, *5*, 1.
[6] A. A. Serga, A. V. Chumak, B. Hillebrands, *J. Phys. D: Appl. Phys.* **2010**, *43*, 264002.
[7] J. J. Bauer, E. R. Rosenberg, C. A. Ross, *Appl. Phys. Lett.* **2019**, *114*, 052403.
[8] O. Ciubotariu, A. Semisalova, K. Lenz, M. Albrecht, *Sci. Rep.* **2019**, *9*, 174741.
[9] C. Hauser, T. Richter, N. Homonnay, C. Eisenschmidt, M. Qaid, H. Deniz, D. Hesse, M. Sawicki, S. G. Ebbinghaus, G. Schmidt, *Sci. Rep.* **2016**, *6*, 20827.
[10] G. Schmidt, C. Hauser, P. Trempler, M. Paleschke, E. T. Papaioannou, *Phys. Status Solidi B* **2020**, *257*, 1900644.
[11] J. Fu, M. Hua, X. Wen, M. Xue, S. Ding, M. Wang, P. Yu, S. Liu, J. Han, C. Wang, H. Du, *Appl. Phys. Lett.* **2017**, *110*, 202403.
[12] J. Ding, C. Liu, Y. Zhang, U. Erugu, Z. Quan, R. Yu, E. McCollum, S. Mo, S. Yang, H. Ding, X. Xu, *Phys. Rev. Appl.* **2020**, *14*, 014017.
[13] L. Soumah, N. Beaulieu, L. Qassym, C. Carrétéro, E. Jacquet, R. Lebourgeois, J. B. Youssef, P. Bortolotti, V. Cros, A. Anane, *Nat. Commun.* **2018**, *9*, 3355.
[14] Y. Lin, L. Jin, H. Zhang, Z. Zhong, Q. Yang, Y. Rao, M. Li, *J. Magn. Magn. Mater.* **2020**, *496*, 165886.
[15] H. T. Nembach, T. J. Silva, J. M. Shaw, M. L. Schneider, M. J. Carey, S. Maat, J. R. Childress, *Phys. Rev. B* **2011**, *84*, 054424.
[16] H. Chen, P. D. Gasperis, R. Marcelli, M. P. Horvath, R. McMichael, P. E. Wigen, *J. Appl. Phys.* **1990**, *67*, 5530.
[17] L. Caretta, S. H. Oh, T. Fakhrul, D. K. Lee, B. H. Lee, S. K. Kim, C. A. Ross, K. J. Lee, *Science* **2020**, *370*, 1438.
[18] T. Fakhrul, S. Tazlaru, L. Beran, Y. Zhang, M. Veis, C. A. Ross, *Adv. Opt. Mater.* **2019**, *7*, 1900056.
[19] Y. Fan, M. J. Gross, T. Fakhrul, J. Finley, J. T. Hou, S. Ngo, L. Liu, C. A. Ross, *Nat. Nanotechnol.* **2023**, 1.
[20] N. Adachi, V. P. Denysenkov, S. I. Khartsev, A. M. Grishin, T. Okuda, *J. Appl. Phys.* **2000**, *88*, 2734.
[21] B. Khurana, J. J. Bauer, P. Zhang, T. Safi, C. T. Chou, J. T. Hou, T. Fakhrul, Y. Fan, L. Liu, *Phys. Rev. Mater.* **2021**, *5*, 084408.
[22] L. Caretta, E. Rosenberg, F. Büttner, T. Fakhrul, P. Gargiani, M. Valvidares, Z. Chen, P. Reddy, D. A. Muller, C. A. Ross, G. S. Beach, *Nat. Commun.* **2020**, *11*, 1090.
[23] P. Hansen, K. Witter, W. Tolksdorf, *Phys. Rev. B* **1983**, *27*, 6608.
[24] H. Callen, *Mater. Res. Bull.* **1971**, *6*, 931.
[25] R. Wolfe, R. C. LeCraw, S. L. Blank, R. D. Pierce, *AIP Conf. Proc.* **1976**, *34*, 172.
[26] P. Hansen, C.-P. Klages, J. Schuldt, K. Witter, *Phys. Rev. B* **1985**, *31*, 5858.
[27] V. J. Fratello, S. E. G. Slusky, C. D. Brandle, M. P. Norelli, *J. Appl. Phys.* **1986**, *60*, 2488.
[28] H. Callen, *Appl. Phys. Lett.* **1971**, *18*, 311.
[29] E. R. Rosenberg, K. Litzius, J. M. Shaw, G. A. Riley, G. S. Beach, H. T. Nembach, C. A. Ross, *Adv. Electron. Mater.* **2021**, *7*, 2100452.
[30] P. Hansen, C.-P. Klages, K. Witter, *J. Appl. Phys.* **1986**, *60*, 721.
[31] L. C. Luther, R. C. LeCraw, J. J. F. Dillon, R. Wolfe, *J. Appl. Phys.* **1982**, *53*, 2478.
[32] V. J. Fratello, S. E. G. Slusky, C. D. Brandle, M. P. Norelli, *J. Appl. Phys.* **1986**, *60*, 718.
[33] E. Y. Vedmedenko, A. Kubetzka, K. Von Bergmann, O. Pietzsch, M. Bode, J. Kirschner, H. P. Oepen, R. Wiesendanger, *Phys. Rev. Lett.* **2004**, *92*, 077207.
[34] K. W. Moon, J. W. Choi, C. Kim, J. Yoon, D. O. Kim, K. M. Song, B. S. Chun, D. Kim, C. Hwang, *Phys. Rev. Appl.* **2018**, *10*, 064014.
[35] V. J. Fratello, S. J. Licht, C. D. Brandle, H. M. O'Bryan, F. A. Baiocchi, *J. Cryst. Growth* **1994**, *142*, 93.
[36] K. Machida, Y. Asahara, *J. Magn. Soc. Jpn.* **1987**, *11*, S1_347.
[37] D. C. Miller, R. Caruso, *J. Cryst. Growth* **1974**, *27*, 274.
[38] J. H. V. D. Merwe, *J. Appl. Phys.* **1963**, *34*, 123.
[39] F. Büttner, M. A. Mawass, J. Bauer, E. Rosenberg, L. Caretta, C. O. Avci, J. Gräfe, S. Finizio, C. A. F. Vaz, N. Novakovic, M. Weigand, *Phys. Rev. Mater.* **2020**, *4*, 011401.
[40] H. T. Nembach, T. J. Silva, J. M. Shaw, M. L. Schneider, M. J. Carey, S. Maat, J. R. Childress, *Phys. Rev. B* **2011**, *84*, 054424.
[41] Y. Ding, T. J. Klemmer, T. M. Crawford, *J. Appl. Phys.* **2004**, *96*, 2969.
[42] I. Neudecker, G. Woltersdorf, B. Heinrich, T. Okuno, G. Gubbiotti, C. H. Back, *J. Magn. Magn. Mater.* **2006**, *307*, 148.
[43] S. S. Kalarickal, P. Krivosik, M. Wu, C. E. Patton, M. L. Schneider, P. Kabos, T. J. Silva, J. P. Nibarger, *J. Appl. Phys.* **2006**, *99*, 093909.
[44] N. Nakamura, H. Ogi, M. Hirao, T. Fukuhara, K. Shiroki, N. Imaizumi, *Jpn. J. Appl. Phys.* **2008**, *47*, 3851.
[45] C. N. Wu, C. C. Tseng, Y. T. Fanchiang, C. K. Cheng, K. Y. Lin, S. L. Yeh, S. R. Yang, C. T. Wu, T. Liu, M. Wu, M. Hong, *Sci. Rep.* **2018**, *8*, 1108.
[46] R. O. Handley, *Modern Magnetic Materials: Principles and Applications*, John Wiley & Sons, New York, NY **1999**.
[47] C. O. Avci, A. Quindeau, C. F. Pai, M. Mann, L. Caretta, A. S. Tang, M. C. Onbasli, C. A. Ross, G. S. Beach, *Nat. Mater.* **2017**, *16*, 309.
[48] K. Garello, I. M. Miron, C. O. Avci, F. Freimuth, Y. Mokrousov, S. Blügel, S. Auffret, O. Boulle, G. Gaudin, P. Gambardella, *Nat. Nanotechnol.* **2013**, *8*, 587.

[49] C. Hahn, G. D. Loubens, O. Klein, M. Viret, V. V. Naletov, J. B. Youssef, *Phys. Rev. B* **2013**, *87*, 174417.
[50] Y. T. Chen, S. Takahashi, H. Nakayama, M. Althammer, S. T. Goennenwein, E. Saitoh, G. E. Bauer, *Phys. Rev. B* **2013**, *87*, 144411.
[51] E. R. Rosenberg, L. Beran, C. O. Avci, C. Zeledon, B. Song, C. G. Fuentes, J. Mendil, P. Gambardella, M. Veis, C. Garcia, G. S. Beach, *Phys. Rev. Mater.* **2018**, *2*, 094405.
[52] J. J. Bauer, E. R. Rosenberg, S. Kundu, K. A. Mkhoyan, P. Quarterman, A. J. Grutter, B. J. Kirby, J. A. Borchers, C. A. Ross, *Adv. Electron. Mater.* **2020**, *6*, 1900820.
[53] L. Liu, T. Moriyama, D. C. Ralph, R. A. Buhrman, *Phys. Rev. Lett.* **2011**, *106*, 036601.
[54] A. J. Berger, E. R. Edwards, H. T. Nembach, O. Karis, M. Weiler, T. J. Silva, *Phys. Rev. B* **2018**, *98*, 024402.